The Astrophysical Journal, 908:153 (8pp), 2021 February 20 https://doi.org/10.3847/1538-4357/abd08a

Modeling of the ALMA HL Tau Polarization by Mixture of Grain Alignment and Self-scattering

Tomohiro Mori[1] and Akimasa Kataoka[2]
[1] The Institute of Astronomy, the University of Tokyo, 2-21-1 Osawa, Mitaka, Tokyo 181-8588, Japan
[2] National Astronomical Observatory of Japan, 2-21-1 Osawa, Mitaka, Tokyo 181-8588, Japan; aki.kataoka.astro@gmail.com
Received 2020 March 26; revised 2020 December 1; accepted 2020 December 2; published 2021 February 19

Abstract

Dust polarization at (sub)millimeter wavelengths has been observed for many protoplanetary disks. Theoretically, multiple origins potentially contribute to the polarized emission but it is still uncertain what mechanism is dominant in disk millimeter polarization. To quantitatively address the origin, we perform radiative transfer calculations of the mixture of alignment and self-scattering-induced polarization to reproduce the 3.1 mm polarization of the HL Tau disk, which shows azimuthal pattern in polarization vectors. We find that a mixture of the grain alignment and self-scattering is essential to reproduce the HL Tau 3.1 mm polarization properties. Our model shows that the polarization of the HL Tau at 3.1 mm can be decomposed to be the combination of the self-scattering parallel to the minor axis and the alignment-induced polarization parallel to the major axis, with the orders of $\sim 0.5\%$ fraction for each component. This slightly eases the tight constraints on the grain size of $\sim 70\ \mu$m to be $\sim 130\ \mu$m in the previous studies but further modeling is needed. In addition, the grain alignment model requires effectively prolate grains but the physics to reproduce it in protoplanetary disks is still a mystery.

Unified Astronomy Thesaurus concepts: Protoplanetary disks (1300); Planet formation (1241); Circumstellar dust (236); Millimeter astronomy (1061); Dust continuum emission (412); Polarimetry (1278)

1. Introduction

The presence of dust polarization of protoplanetary disks at submillimeter/millimeter wavelengths has been indicated for several protostars and T Tauri stars with the James Clerk Maxwell Telescope (JCMT) single-channel polarimeter (Akeson & Carlstrom 1997; Tamura et al. 1995, 1999). However, for two decades, spatially resolved polarization has not been obtained due to the lack of the sensitivity and spatial resolutions of the instruments (Hughes et al. 2009, 2013) until the first detection of the millimeter polarization for the HL Tau disk by Stephens et al. (2014). Nowadays, ALMA dust polarization observations have enabled us to obtain the polarization for various class II protoplanetary disks, showing the various polarization morphology and polarization fractions (Kataoka et al. 2016b, 2017; Stephens et al. 2017; Bacciotti et al. 2018; Hull et al. 2018; Ohashi et al. 2018; Dent et al. 2019; Harrison et al. 2019; Mori et al. 2019).

One difficulty in interpreting the disk polarization is that multiple mechanisms of polarization are at work at millimeter wavelengths. One mechanism is the grain alignment, where elongated dust grains are aligned to some directions and emit polarized thermal dust emission. The grain alignment mechanism has been long and well studied, especially the radiative torques (RATs) (e.g., Lazarian & Hoang 2007). Here we only discuss which direction the grains are aligned to because it reflects the polarization orientation. The directions of the grain alignment may represent magnetic fields (Davis & Greenstein 1951; Cho & Lazarian 2007), radiation (Tazaki et al. 2017), or gas flow (Gold 1952; Lazarian & Hoang 2007; Kataoka et al. 2019). Since the grain alignment has been mainly studied in the condition of the interstellar medium, further discussion of the alignment physics in the protoplanetary disks is necessary. Another mechanism that would produce polarization is the self-scattering, where the dust grains scatter and polarize the incoming thermal emission from other dust grains (Kataoka et al. 2015). Dust grains with the size comparable to observed wavelengths efficiently scatter and polarize the thermal emission. The interpretations of the observations depend on each target. However, the interpretation itself is one of the major issues of the millimeter polarization of protoplanetary disks.

To interpret the dust polarization, it is essential to disentangle the polarization mechanisms. In this paper, as one step toward complete understanding of the polarization, we investigate the effects of superposition of the two major polarization mechanisms, which are the self-scattering and alignment. Especially, we model the 3.1 mm polarization of the HL Tau disk, which has been interpreted purely as alignment-induced polarization (Kataoka et al. 2017), but also pointed out to be contaminated by self-scattering (Yang et al. 2019).

HL Tau is a class I/II protostar in the Taurus star-forming complex at a distance of 140 pc from the solar system (Rebull et al. 2004; Robitaille et al. 2007). A notable feature of the surrounding disk is the concentric multi-ringed structure with a spatial scale of ∼100 au (ALMA Partnership et al. 2015). The polarization morphology at millimeter wavelengths on the HL Tau disk shows strong wavelength dependence (Stephens et al. 2014; Kataoka et al. 2017; Stephens et al. 2017). The polarization morphology at 870 μm is parallel to the disk minor axis, while that at 3.1 mm shows almost the azimuthal pattern. The polarization pattern with the vectors parallel to the minor axis is well reproduced by the self-scattering model (Kataoka et al. 2016a; Yang et al. 2016). Therefore, the 870 μm polarization has been interpreted by the self-scattering. In contrast, the origin of the 3.1 mm polarization has been interpreted by dust alignment because the self-scattering fails to explain the azimuthal pattern. It has been first interpreted by grain alignment with the radiative anisotropy (Kataoka et al. 2017; Tazaki et al. 2017), but slight inconsistency in the morphology has also been pointed out (Yang et al. 2019).

The switching of the polarization mechanisms between 870 μm and 3.1 mm must be explained. That the self-scattering disappears at 3.1 mm is an expected behavior because polarization fraction

quickly drops if dust grains are larger than the wavelengths divided by 2π (Kataoka et al. 2015). However, this requires the grain size to be $\sim$100 μm, which is not consistent with the general SED analysis, which requests millimeter to centimeter dust grains (e.g., Beckwith & Sargent 1991; Ricci et al. 2010). Carrasco-González et al. (2019) analyzed the millimeter SED of the HL Tau disk with the effects of scattering-induced intensity reduction (Liu 2019; Zhu et al. 2019) and obtained grain size to be millimeter, which is larger than $\sim$100 μm. In contrast, the reason why alignment-induced polarization is observed at 3.1 mm but disappears at 870 μm is still unresolved. One idea to explain the transition is that the grain size is comparable to the wavelengths, and their intrinsic polarization is strong enough to be detected at 3.1 mm but too weak at 870 μm. This happens because of the transition from Rayleigh to Mie regime. If the grain size is much smaller than the wavelengths, the intrinsic polarization does not have strong wavelength dependence. If the grain size is much larger than the wavelengths, in contrast, the polarization fraction drops. Note that if the grain size is comparable to the wavelengths, polarization direction becomes perpendicular to the grain major axis because of the Mie regime (e.g., Guillet et al. 2020). In this way, the wavelength dependence between millimeter and submillimeter wavelengths is the key to understanding the polarization.

Toward the full understanding of the wavelength-dependent polarization of the HL Tau, in this paper, we focus on the modeling the 3.1 mm polarization by the mixture of the self-scattering and grain alignment. Yang et al. (2019) raised the issue that neither aerodynamic nor radiative flux induced polarization can explain the 3.1 mm polarization, and speculated on possible contamination of the self-scattering component. We quantitatively investigate how strong the self-scattering contamination is even at the 3.1 mm band and leave the full modeling of the three wave bands for future studies. Note that this does not solve the issue that no alignment model can perfectly explain the polarization, but it may change the wavelength dependence of the self-scattering components in the HL Tau polarization, which may have an impact on the grain size constraints.

2. Model

We briefly describe the outline of the radiative transfer models in this study. First, we construct a dust disk model that reproduces the Stokes I emission obtained with the 3.1 mm polarization observation. Then, on the constructed disk model, we take into account the effect of the grain alignment and self-scattering in calculating polarization.

2.1. Disk Model

Figure 1 shows the Stokes I intensity, polarized intensity, and polarization fraction, all of which are overlaid with the polarization vectors. The notable features of the 3.1 mm polarization are (1) azimuthal polarization morphology and (2) azimuthally uniform polarization fraction at $\sim$1%.

We construct an axisymmetric disk model that reproduces the stokes I image obtained on the polarization observation at 3.1 mm (Kataoka et al. 2017; Stephens et al. 2017). By assuming that the Stokes I emission at 3.1 mm is optically thin, we construct the radial profile of the optical depth at 3.1 mm with the form of

$$\tau_{\rm model}(r) = \tau_0 \left(\frac{r}{1\ {\rm au}}\right)^{-\gamma_1} \exp\left[\left(\frac{r}{r_c}\right)^{-\gamma_2}\right], \quad (1)$$

with the temperature profile of $T(r) = 310(r/1\ {\rm au})^{-0.57}$ K (Okuzumi & Tazaki 2019). We note that both the dust surface density and temperature are assumed to have smooth radial distributions without any ring and gap structures observed with the higher spatial resolution (ALMA Partnership et al. 2015) for simplicity.

We adopt the parameter set of $(\tau_0, r_c, \gamma_1, \gamma_2) = (1.0, 129.2, 6.6, 9.0)$, which reproduces the Stokes I emission. Figure 2 shows the images of observed and modeled Stokes I produced assuming the parameter set and residual.

We derive the dust surface density profile $\Sigma_d(r)$ by calculating $\Sigma_d(r) = \tau_{\rm model}/\kappa_{\rm abs}$, where $\kappa_{\rm abs}$ is the absorption opacity. As we will describe below, the value of $\kappa_{\rm abs}$ is a function of $a_{\rm max}$ and λ when constituent materials are determined. For the fiducial value, we adopt $\kappa_{\rm abs}(a_{\rm max} = 100\ \mu{\rm m}, \lambda = 3.1\ {\rm mm}) = 0.0788\ {\rm cm^2\ g^{-1}}$ in calculating the dust surface density.

The vertical dust density is assumed to be Gaussian density distribution with a dust scale height h_d such that $\rho_d = \Sigma_d/\sqrt{2\pi}\, h_d \exp(-z^2/2h_d^2)$. We also assume that h_d is the same as the gas pressure scale height.

While the residuals are still significant, they show axisymmetric distribution. For this study, we aim at reproducing the continuum emission with an axisymmetric model for simplicity, and thus we do not further search the parameter sets.

2.2. Dust Model

We use a grain composition model developed by Birnstiel et al. (2018), where the grains are the mixture of silicate, troilite, organics, and water ice. The refractive index used in the calculation is as follows: Draine (2003) for astronomical silicate, Henning & Stognienko (1996) for troilite and refractory organics, and Warren & Brandt (2008) for water ice. We compute the mixture of them with the effective medium theory using the Maxwell–Garnett rule (e.g., Bohren 1983; Miyake & Nakagawa 1993). We assume the grains have a power-law-size distribution with a power of $q = -3.5$ (Mathis et al. 1977) with the maximum grain size of $a_{\rm max}$, while the minimum grain size is fixed at $a_{\rm min} = 0.05\ \mu$m. We assume the same grain population throughout the disk.

To reproduce polarization, we consider both alignment and scattering-induced polarization. For the alignment-induced polarization, we consider both prolate and oblate grains.[3] The motivation to consider both models is the observed polarization morphology. There are two ways to reproduce azimuthal polarization vectors; effectively prolate grains with their major axis parallel to the disk azimuthal direction and effectively oblate grains with their minor axis parallel to the disk radial direction. We assume the Rayleigh regime (Lee & Draine 1985) to calculate the intrinsic polarization. This approximation holds when the size parameter $x = 2\pi a/\lambda \ll 1$. We assume the grain size up to 200 μm at the wavelength of 3.1 mm, which corresponds to the size parameter of $x = 0.42$, which justifies the use of Rayleigh regime. We assume the axes ratio of the

[3] Grains are believed to be spinning when they are aligned. The spinning motion makes the grains effectively prolate or oblate ellipsoidal bodies. We call grains prolate/oblate for simplicity but this does not rule out any complex shapes of the dust grains.

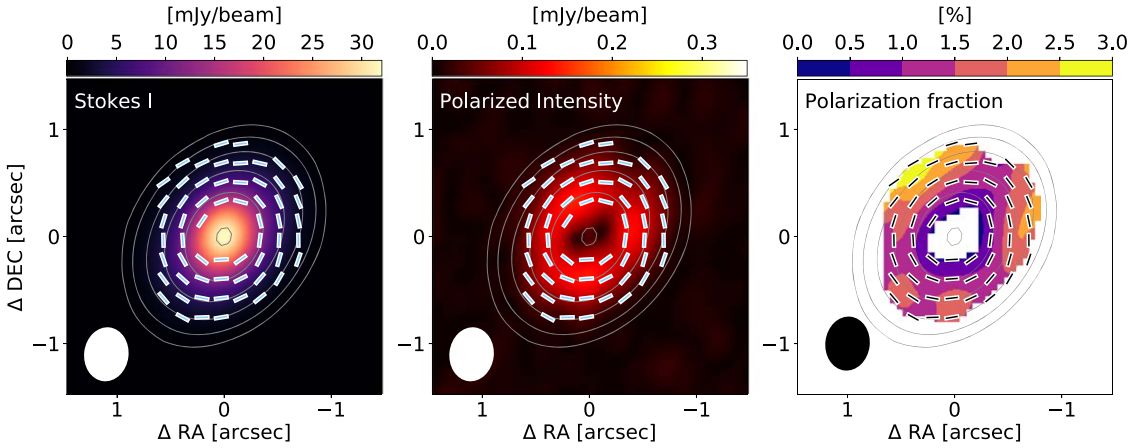

Figure 1. ALMA Band 3 ($\lambda = 3.1$ mm) polarimetric observations of the HL Tau disk, which has been previously reported by Kataoka et al. (2017) and Stephens et al. (2017). The left panel shows the Stokes I intensity in color, the central panel shows the polarized intensity, and the right panel shows the polarization fraction. The solid contours in the three panels are equivalent and represent the intensity with the levels of (10, 25, 60, 150, 366, 900) times the noise level, which is σ_I (=34 μJy beam^{-1}). The overlaid line segments represent the polarization vectors where the polarized intensity is larger than three times the noise level of the polarized intensity, which is $\sigma_{\rm PI}$ (=5.3 μJy beam^{-1}). Note that the length of the polarization vectors is set to be equal. The beam has a size of $0\farcs51 \times 0\farcs41$ and position angle of $-6\fdg76$, which is represented in the bottom left as an ellipse.

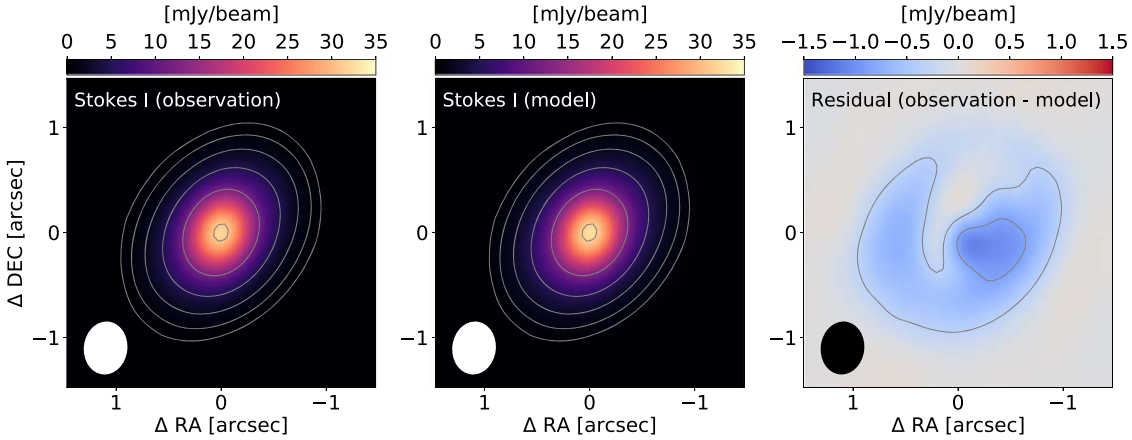

Figure 2. The left panel shows the Stokes I image of the observations, the central panel shows the model image, and the right panel shows the residual map where the observed Stokes I subtracted from the model image. The contours of the left and the central panels are the same as Figure 1 and the contour of the right panel shows the residual levels of $(-10, -25) \times \sigma_I$.

grains to be $\alpha = 0.9$ for prolate grains and $\alpha = 1.1$ for oblate grains and that the alignment efficiency is $\epsilon = 0.6$. We assume that the oblate grains are aligned with their short axis parallel to the radial direction of the disk while the prolate grains are aligned with their long axis parallel to the azimuthal direction of the disk. We ignore the effects of temperature for simplicity.

As pointed out by Guillet et al. (2020), to discuss the wavelength dependence of the alignment-induced polarization, the Mie regime is essential to be considered. In this paper, however, we do not treat the Mie regime for simplicity and we focus on the single band observations on the HL Tau at 3.1 mm. In the cases of further modeling at 870 μm and at 1.3 mm, the Mie regime treatment is required because the size parameter of 200 μm grains becomes $x = 1.44$ at 870 μm and $x = 0.97$ at 1.3 mm.

The scattering-induced polarization is included by turning on the scattering in the radiative transfer simulations. We treat the full phase function and take into account the multiple scattering. The controlling parameter of the scattering is the maximum grain size, $a_{\rm max}$. The self-scattering polarization is the most effective when the maximum grain size is $a_{\rm max} \sim \lambda/2\pi$ (Kataoka et al. 2015). We assume spherical dust grains for computing self-scattering while we assume oblate or prolate grains for computing alignment-induced polarization. These are not consistent but we neglect the effects of scattering by non-spherical grains for simplicity. The angle-averaged absorption opacity of oblate/prolate grains is set to be the same as the spherical grains.

We also note a technical treatment. The radiative transfer code RADMC-3D allows users to compute the alignment-induced polarization only when the dust scattering is turned on. To reproduce the alignment-induced polarization without scattering, therefore, we use $a_{\rm max} = 50\,\mu$m with the scattering turned on, where the scattering-induced polarization is negligible.

3. Results

3.1. Alignment-only Model

First, we see how the beam dilution affects the appearance of the polarization vectors. We use the same disk model of HL Tau but assume that the disk is observed with a face-on view, $i = 0°$. The left panels of Figure 3 demonstrate the effects of beam dilution with the face-on view. To reproduce the azimuthal polarization pattern, the prolate grains are assumed

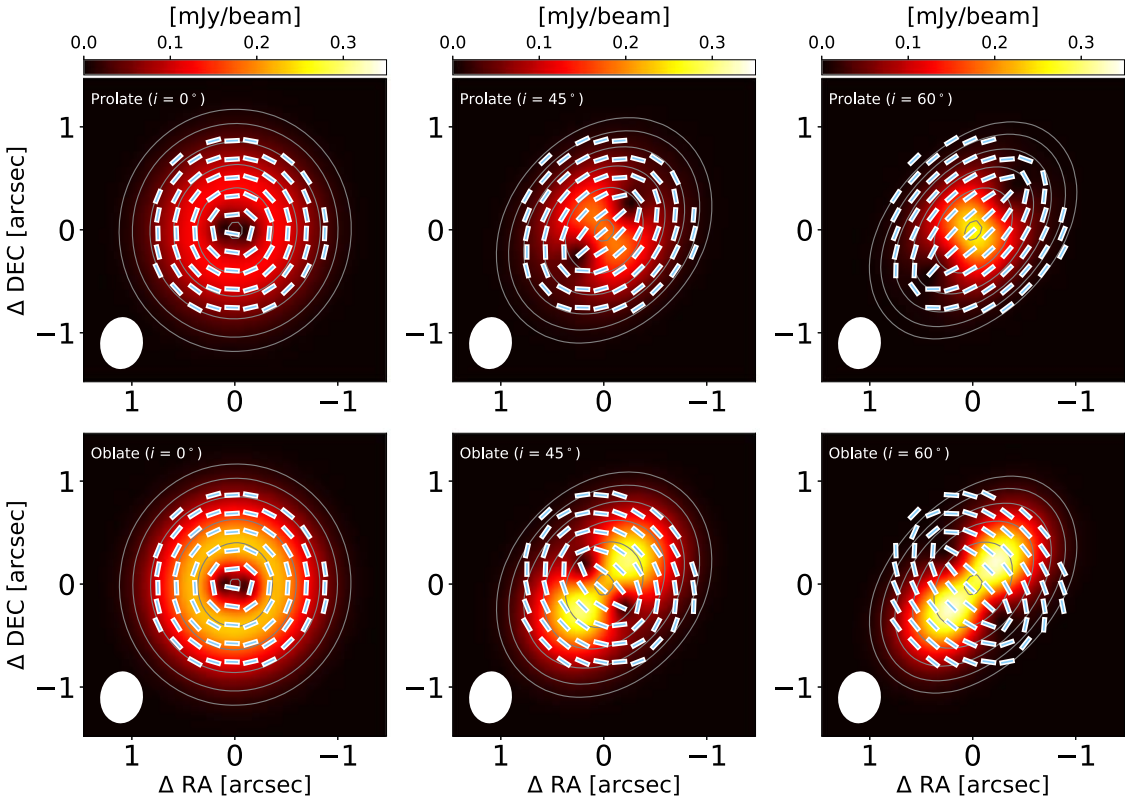

Figure 3. The six panels show the polarized intensity of models with prolate and oblate grains with different disk inclinations. The top three panels show the results of the prolate grains with their long axis parallel to the azimuthal direction and the disk inclinations are $i = 0°$ (left), 45° (center), and 60° (right). The bottom three panels show the same as the top but for oblate grains. The levels of contours and the line segments are the same as Figure 1 but for each model. The synthesized beam is represented as the ellipse at the bottom left of each panel.

to be aligned with their long axis parallel to the azimuthal direction, while the oblate grains are with their short axis parallel to the radial direction. Both models generally show the azimuthal pattern in polarization vectors, but the vectors at around the central region have certain inclination angles, which is not expected in the case without beam dilution.

Next, we see the effects of changing the disk inclination angle on the appearance of the polarization vectors and polarized intensity. The center and right columns of Figure 3 show the case of the inclination angles of 45°, and 60°. The polarization vectors are almost in the azimuthal directions in the inclination angles of 45° and 60° for both the prolate and oblate grains, except in the central regions where the beam dilution affects the morphology.

Yang et al. (2019) proposed that, if the disk inclination is non-zero, we can distinguish the alignment models between effectively prolate and oblate grains by investigating if the polarization vectors are in the azimuthal directions (i.e., azimuthal pattern) or are with their normal direction toward the disk center (i.e., circular pattern). However, as we see in Figure 3, the difference between elliptical and circular patterns is hard distinguish because of the beam dilution.

In contrast, the polarized intensity shows prominent differences between the prolate and oblate grain models; the prolate grain models show higher polarized intensity (i.e., brighter color in Figure 3) along the minor axis than along the major axis, while the oblate models show higher polarized intensity along the major axis. The reason can be understood by simple geometry. Prolate grains along the disk minor axis always show the longest axis in the observed projected plane even if the disk inclination is changed, while those along the disk major axis show less polarization fraction if the disk inclination changes to be closer to edge-on view because of the projection effects. The situation is completely opposite in the case of oblate grains. Oblate grains along the disk major axis always show the longest axis to observers while those along the minor axis become fainter in higher inclination angles because of the projection effects. Therefore, investigating the polarized intensity pattern is a promising way to distinguish the mechanisms between prolate and oblate models if the polarization is purely due to the grain alignment.

Now we come back to the case of the HL Tau disk. As shown in the central panel of Figure 1, the polarized intensity of the HL Tau disk at 3.1 mm wavelength shows little variation in the azimuthal direction. This is different from the models that we discussed, where the prolate grain model shows that polarized intensity is brighter along the disk minor axis while the oblate model shows it is brighter along the disk major axis. This illustrates that alignment-only models may not be able to reproduce the observed polarized intensity pattern. This motivates us to add another mechanism of polarization, self-scattering, which we will discuss in the next chapter.

We note that the general properties described above hold for the polarization fraction as shown in Figure 5 in the Appendix. In addition, the general behavior and differences between prolate and oblate grain models is also discussed by Yang et al. (2019) with semi-analytical models.

3.2. Mixture of Alignment and Scattering Models

Next, we discuss a possibility that a mixture of the alignment and self-scattering models can reproduce the HL Tau polarization

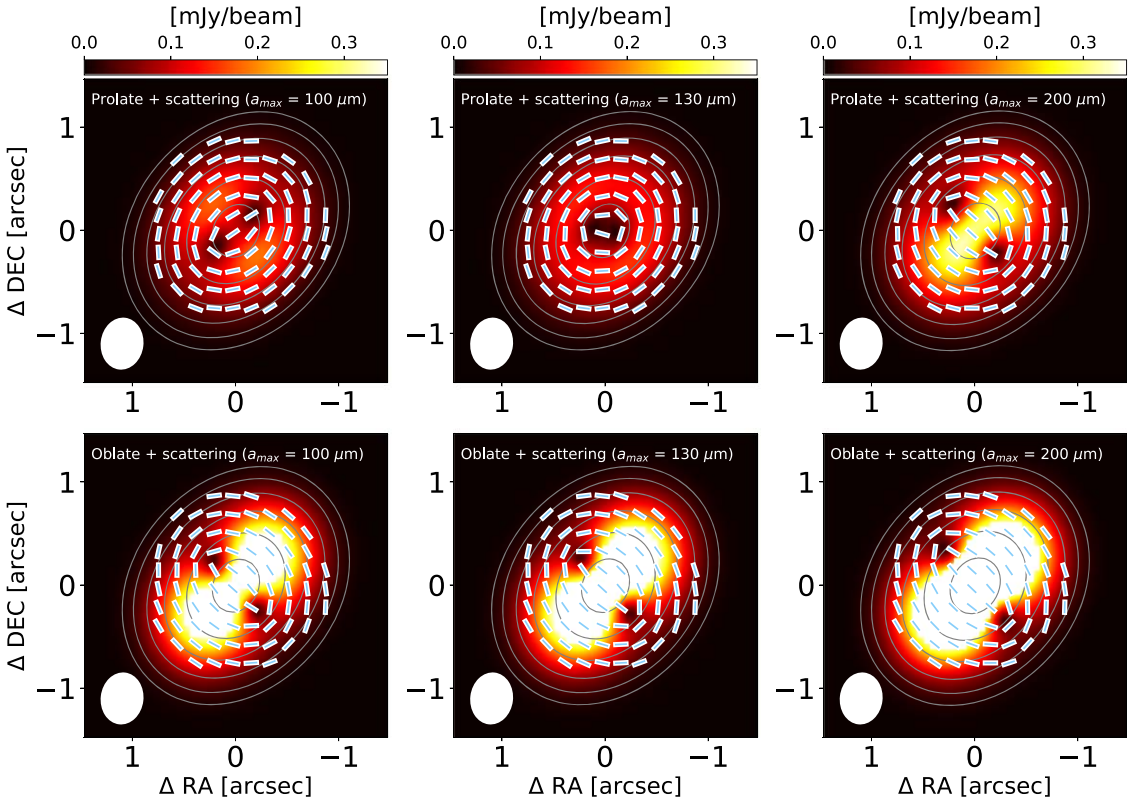

Figure 4. The six panels show the polarized intensity of models with mixture of the grain alignment and self-scattering. The upper three panels show the case of the combination of the aligned prolate grain and self-scattering. The prolate grain model is fixed through the three panels while the self-scattering-induced polarization is changed by setting the maximum grain size to be $a_{\rm max} = 100$ μm (left), 130 μm (center), and 200 μm (right). Note that the contribution of self-scattering is weaker for the left panel and stronger for the right panel. The bottom panels are the same as the top panels but for oblate grains.

at 3.1 mm. The self-scattering polarization generally produces the polarization vectors parallel to the minor axis, and the fraction is a strong function of the grain size. Therefore, we set the maximum grain size $a_{\rm max}$ to be the the major parameter and change it to reflect the strength of the self-scattering polarization. We use the same disk models of the alignment-induced polarization of the prolate and oblate cases, and add the self-scattering-induced polarization.

Figure 4 shows the polarized intensity of the prolate and oblate grain models with $i = 45°$. The contributions of the self-scattering model increase by increasing $a_{\rm max}$ from left to right panels while that of the alignment models is fixed.

As expected, the oblate + scattering models do not reproduce the observation. Both polarization of the alignment of oblate grains and self-scattering produces stronger polarization along the major axis. As a result of superposition, the azimuthal variation becomes stronger, which is not consistent with the observation shown in Figure 1, which shows little azimuthal variation in polarized intensity. Instead, the prolate + scattering model shows less azimuthal variation than the oblate + scattering model. This is because the prolate grain alignment produces strong polarization along the disk major axis while the self-scattering does so along the disk minor axis. As a result of their superposition, the polarized intensity shows less azimuthal variation, which is consistent with the observations.

Now the question is, how strong are the contributions of the alignment and scattering? We focus on the prolate + scattering model and discuss it. The top three panels of Figure 4 show the case of different grain sizes, which correspond to difference of contribution of self-scattering. As demonstrated in the figure, the $a_{\rm max} = 100\,\mu$m case is dominated by the alignment-induced polarization because the polarized intensity is stronger along the minor axis, while the $a_{\rm max} = 200\,\mu$m is by the self-scattering because it is stronger along the major axis. The $a_{\rm max} = 130\,\mu$m case shows the half-and-half contributions between alignment and scattering, which reproduce little azimuthal variation as observed. Therefore, we conclude that prolate + scattering model with $a_{\rm max} = 130\,\mu$m best reproduces the observed HL Tau polarization at 3.1 mm. Note that we also successfully reproduce the observed polarization fraction with the mixture model $a_{\rm max} = 130\,\mu$m as shown in Figure 5 in the Appendix.

4. Discussion

The main results of the radiative transfer calculations are: (1) the HL Tau 3.1 mm polarization can be reproduced with the mixture of the alignment and self-scattering models; and (2) the prolate grain model can explain the observations but the oblate model does not. In this section, we discuss the implications on the grain properties from both alignment and scattering theories as well as the caveats of our models.

4.1. What Can Reproduce Effectively Prolate Shape?

As discussed also by Yang et al. (2019), the effectively prolate grain model is preferable for reproducing the HL Tau polarization but it is theoretically counter-intuitive. We usually assume that grains are spinning if they are aligned, and they are observed as effectively oblate grains.

One possible speculation for explaining the prolate grain model is that grains are not spinning in the HL Tau disk. The

Table 1
Summary of the Total Polarization Fraction of the Models and Observations

	λ (mm)	PF_{total}($\simeq PF_{scat} + PF_{align}$) (%)	PF_{scat} (%)	PF_{align} (%)
oblate	3.1	1.07	0	1.07
oblate + scattering ($a_{max} = 100\ \mu$m)	3.1	1.25	0.20	1.07
oblate + scattering ($a_{max} = 130\ \mu$m)	3.1	1.47	0.42	1.07
oblate + scattering ($a_{max} = 200\ \mu$m)	3.1	2.23	1.21	1.07
prolate	3.1	−0.55	0	−0.55
prolate + scattering ($a_{max} = 100\ \mu$m)	3.1	−0.35	0.20	−0.55
prolate + scattering ($a_{max} = 130\ \mu$m)	3.1	−0.12	0.42	−0.55
prolate + scattering ($a_{max} = 200\ \mu$m)	3.1	0.68	1.21	−0.55
observation	3.1	$-0.1 < PF_{total} < 0.1$	⋯	⋯
observation	1.3	0.551 ± 0.003	⋯	⋯
observation	0.87	0.619 ± 0.004	⋯	⋯

Note. The first column represents the model names. λ is the wavelengths. PF_{total} represents the total polarization fraction, which can be decomposed to the scattering component, PF_{scat} and the alignment component, PF_{align}. We define positive values of the polarization fraction for the component parallel to the disk minor axis and negative values for that parallel to the disk major axis.

only mechanism that does not assume grain spinning so far would be the mechanical alignment with a supersonic gas flow, which is so-called Gold alignment, where the long axis of needle-like grains is parallel to the gas flow onto dust grains (Gold 1952). However, the Gold alignment assumes that the gas speed on the dust grains is supersonic, whereas it is generally subsonic in protoplanetary disks (e.g., Cho & Lazarian 2007). All the discussion above is phenomenological and we need further development of general grain alignment theory in protoplanetary disks.

Furthermore, we note that, even if the Gold mechanism is at work, the predicted polarization pattern is not consistent with the observations. The direction of the polarization would be parallel to the gas flow on the frame of dust grains (Kataoka et al. 2019), which is a strong function of the Stokes number, which denotes how well dust grains couple to ambient gas. The grain radius a is found to be $a_{max} = 130\ \mu$m in our modeling, which gives the Stokes number to be $St = 5 \times 10^{-3}$ with the assumption of the gas surface density of $\Sigma_g \sim 20$ g cm^{-2}. With such a small number of St much smaller than unity, the directions of gas velocity on grains would be in the radial directions (see Figure 2 in Kataoka et al. 2019). Note that this discussion holds even for ring-like disks (Mori et al. 2019). However, our modeling has found that the directions of the relative velocity are dominantly in the azimuthal directions, which is incompatible with the theory.

4.2. How Efficient Is the Scattering at 3.1 mm?

The size of dust grains has been constrained by modeling the wavelength dependence of the contribution of the scattering-induced polarization. In the case of HL Tau disk, previous studies have assumed that the Band 7 (0.87 mm) polarization is dominated by self-scattering while Band 3 (3.1 mm) has no contribution of self-scattering, which results in the tight constraint on the grain size being 70 μm in size (Kataoka et al. 2016a, 2017; Yang et al. 2016). However, we have revealed that there is a contribution of self-scattering even for the 3.1 mm polarization. Therefore, we discuss if our modeling changes the interpretation of the grain size in the HL Tau disk.

To estimate the scattering component at each wavelength, as conducted in Kataoka et al. (2017), we compute the total polarization across the HL Tau disk, which is given by

$$PF_{total} = \begin{Bmatrix} 1 & \text{(minor)} \\ -1 & \text{(major)} \end{Bmatrix} \times \sqrt{(\Sigma Q)^2 + (\Sigma U)^2}\, \Sigma I, \qquad (2)$$

where ΣI, ΣQ, and ΣU are the Stokes I, Q, and U emissions integrated for the whole disk. Here, we explicitly define the sign of the total polarization fraction; PF_{total} is positive if the position angle of the total polarization, which is calculated from ΣQ, and ΣU, is closer to the disk minor axis, while PF_{total} is negative if the position angle is closer to the disk major axis. This is motivated to be able to estimate the canceling out effects. In the case of axisymmetric protoplanetary disks, the position angle of polarization is usually parallel to either the disk minor or major axes because of the symmetry. If this is the case, defining sign with respect to the disk minor and major axes helps to see which components dominate the total polarization.

Table 1 summarizes the computed total polarization fraction for the observations and models. We update the total polarization fraction presented in Kataoka et al. (2017), who used the SMA and CARMA data, with the ALMA data in Band 6 and 7 while its upper limit in ALMA 3 is presented as the same as with that study. PF_{total} is calculated from the final images as shown in Figure 4 with Equation (2). We also show $PF_{scat,model}$ and $PF_{align,model}$, which represent the total polarization of the cases where either scattering or alignment model is calculated. As shown in Table 1, the total polarization fraction is nearly equal to the sum of those of the scattering and alignment components. This illustrates the powerful estimation of the total polarization by considering the positive and negative signs of each polarization component.

As shown in Table 1, the oblate grain model always shows the positive value while the prolate grain model shows the negative value, where positive value corresponds to the polarization parallel to the disk minor axis while negative value corresponds to that parallel to the disk major axis. In contrast, the self-scattering always shows positive values because of the disk geometry. To reproduce the tight upper limit on the absolute value of the total polarization fraction as less than 0.1%, the oblate grain model is not favored and the combination of the prolate model and self-scattering is the key.

Here, we emphasize our big assumption that we do not know the wavelength dependency of the alignment-induced polarization, and assume that there is no contribution from alignment polarization at the wavelengths of Bands 6 and 7. To reproduce this, we need to calculate the intrinsic polarization in the Mie regime (Kirchschlager et al. 2019; Guillet et al. 2020), which computationally costs. By assuming that there is no contribution of alignment-induced polarization at Bands 6 and 7, we confirm the decreasing trend of the observed total polarization fraction from 0.87 to 3.1 mm, which has been discussed by Kataoka et al. (2017) partially with the SMA and CARMA results from (Stephens et al. 2014). Furthermore, our study revealed that the non-detection of total polarization at 3.1 mm is explained by the combination of the alignment (−0.55%) and the self-scattering (+0.42%), which requires modification on the wavelength dependence of the self-scattering polarization. However, the contribution of self-scattering to the total polarization at 3.1 mm, which is estimated to be 0.42% in this study, is still smaller than the 0.87 and 1.3 mm total polarization fractions. This means that the decreasing trend of the self-scattering polarization still holds, which supports the idea of ∼100 micron-size grains because the wavelength at which the self-scattering polarization peaks is 0.87 mm or shorter (see Kataoka et al. 2016a, 2017; Yang et al. 2016).

Still, there are significant differences in the size measurements between millimeter-wave polarization and spectral indices. Latest modeling for the continuum emission of the HL Tau disk obtained at multiple wavelengths from 0.9 to 13 mm found the radial gradient of the grain sizes from $a_{\rm max} = 1.5$ mm in the inner region to $a_{\rm max} = 500$ μm in the outer region, which is at least four times larger than that in this study (Carrasco-González et al. 2019). Plenty of differences between the two studies, for example the observation wavelengths, angular resolutions, and modeling methods, can affect the size measurements and partly explain the discrepancy. Another primary difference is assumed to be constituent materials of the dust grains, which determine refractive indices. Because the absolute values of the absorption/scattering opacities and their wavelength dependence are strongly sensitive to the assumption on the composition, this can affect the measurement conducted in both of the studies (Testi et al. 2014). To reconcile the discrepancy, further modeling that assumes the same grain composition and disk parameters should be conducted.

4.3. Caveats

In the radiative transfer calculations, the dust models are not fully consistent between the alignment and scattering models. When we calculate the polarization of aligned elongated grains, we set angle-dependent absorption opacities. However, we assume spherical dust grains that have the same absorption opacities for elongated grains for calculating their scattering because of the difficulties in calculating scattering opacities of non-spherical dust grains.

5. Conclusions

The origin of the polarized emission of the HL Tau disk at 3.1 mm has been debated in previous works. We have focused on the 3.1 mm polarization of HL Tau, which shows the azimuthal pattern of polarization vectors, and have conducted radiative transfer simulations for the 3.1 mm HL Tau polarization. Our main findings are as follows.

1. By radiative transfer simulations, we confirmed that alignment-induced polarization cannot reproduce the 3.1 mm polarization feature of the HL Tau disk as discussed by Yang et al. (2019) with a semi-analytical model.
2. Next, we ran models of the mixture of the grain alignment and self-scattering and found that the combination of the effectively prolate grain emission and self-scattering can reproduce the observations. However, the combination of the effectively oblate grain emission and self-scattering cannot reproduce the polarization. Our model shows that the total polarization fraction at 3.1 mm can be understood by the combination of 0.42% polarization due to the self-scattering, which is parallel to the disk minor axis, and 0.55% of the alignment-induced polarization, which is parallel to the disk major axis.
3. We found that the maximum size of the scattering dust grains is $a_{\rm max} \sim 130$ μm to reproduce the azimuthally uniform polarization fraction. This size is consistent with that obtained on the polarization observation in Bands 6 and 7. However, the size is a few times smaller than that measured by the multi-wavelength continuum analysis (Carrasco-González et al. 2019). We confirmed that effectively prolate grain models are preferable to oblate grain models to reproduce the 3.1 mm polarization of HL Tau. However, the physical model to reproduce the situation is still uncertain.

We note that while the radiative transfer calculations have been performed for explaining the 3.1 mm polarization of the HL Tau disk, further modeling of the multi-wavelength polarization with the results at 870 μm and 1.3 mm is required in future studies. Modeling of the multiband polarization observations will provide the spectrum of alignment and scattering efficiency, which will enable us to further constrain the grain sizes and shapes.

We gratefully thank Ian Stephens for providing us with the analyzed ALMA Band 3 polarization data, which has enabled us to conduct the modeling work. We are also deeply grateful to Takashi Miyata, Takafumi Kamizuka, and Ryou Ohsawa for fruitful discussions for our study. This work is supported by JSPS KAKENHI Numbers 18K13590 and 19H05088. ALMA is a partnership of ESO (representing its member states), NSF (USA) and NINS (Japan), together with NRC (Canada), MOST and ASIAA (Taiwan), and KASI (Republic of Korea), in cooperation with the Republic of Chile. The Joint ALMA Observatory is operated by ESO, AUI/NRAO, and NAOJ.

Facility: ALMA.

Appendix
The Polarization Fraction in the Mixture Models (Alignment + Self-scattering)

Figure 5 shows polarization fraction mixture of the grain alignment and self-scattering. As well as Figure 4 in Section 3, the model with prolate grains and $a_{\rm max} = 130$ μm (top-central panel) successfully reproduces the azimuthally uniform polarization fraction with ∼1%–2%, whereas other models predict significant azimuthal variations.

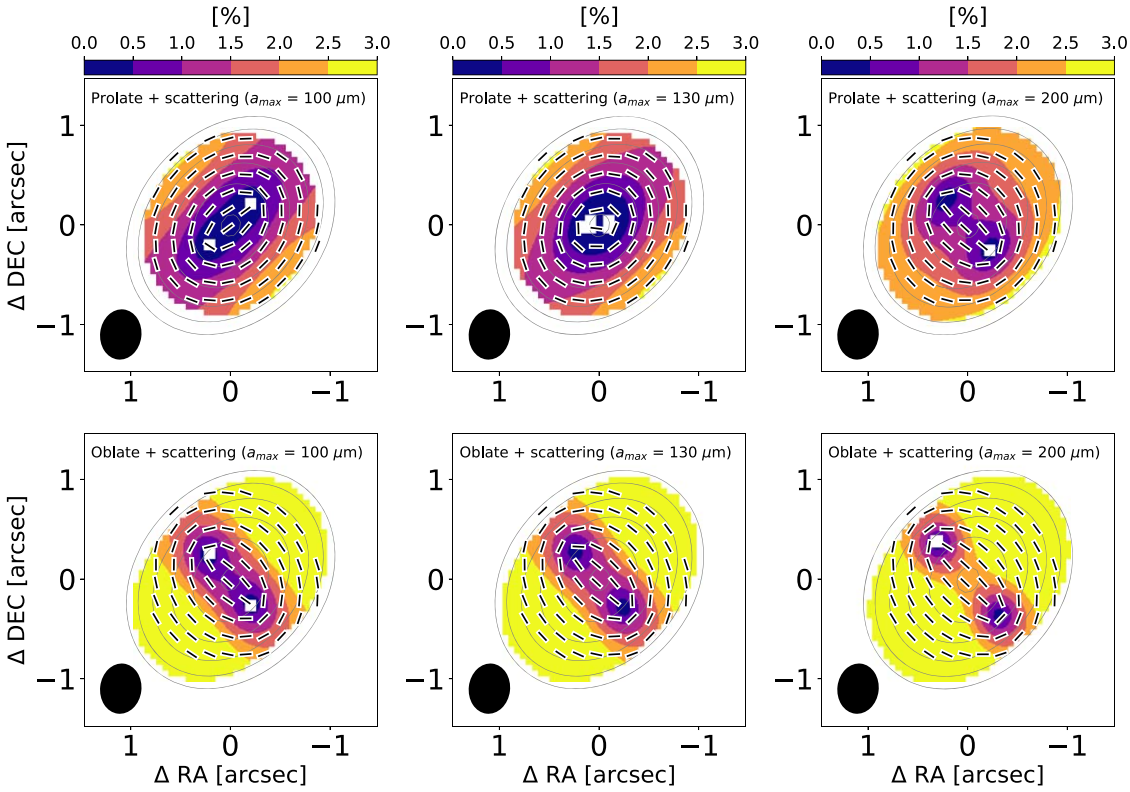

Figure 5. Same as Figure 4, but for polarization fraction.

References

Akeson, R. L., & Carlstrom, J. E. 1997, ApJ, 491, 254
ALMA Partnership, Brogan, C. L., Pérez, L. M., et al. 2015, ApJL, 808, L3
Bacciotti, F., Girart, J. M., Padovani, M., et al. 2018, ApJL, 865, L12
Beckwith, S. V. W., & Sargent, A. I. 1991, ApJ, 381, 250
Birnstiel, T., Dullemond, C. P., Zhu, Z., et al. 2018, ApJL, 869, L45
Bohren, C. F. 1983, TellB, 35B, 65
Carrasco-González, C., Sierra, A., Flock, M., et al. 2019, ApJ, 883, 71
Cho, J., & Lazarian, A. 2007, ApJ, 669, 1085
Davis, L., Jr., & Greenstein, J. L. 1951, ApJ, 114, 206
Dent, W. R. F., Pinte, C., Cortes, P. C., et al. 2019, MNRAS, 482, L29
Draine, B. T. 2003, ARA&A, 41, 241
Gold, T. 1952, MNRAS, 112, 215
Guillet, V., Girart, J. M., Maury, A. J., & Alves, F. O. 2020, A&A, 634, L15
Harrison, R. E., Looney, L. W., Stephens, I. W., et al. 2019, ApJL, 877, L2
Henning, T., & Stognienko, R. 1996, A&A, 311, 291
Hughes, A. M., Hull, C. L. H., Wilner, D. J., & Plambeck, R. L. 2013, AJ, 145, 115
Hughes, A. M., Wilner, D. J., Cho, J., et al. 2009, ApJ, 704, 1204
Hull, C. L. H., Yang, H., Li, Z.-Y., et al. 2018, ApJ, 860, 82
Kataoka, A., Muto, T., Momose, M., et al. 2015, ApJ, 809, 78
Kataoka, A., Muto, T., Momose, M., Tsukagoshi, T., & Dullemond, C. P. 2016a, ApJ, 820, 54
Kataoka, A., Okuzumi, S., & Tazaki, R. 2019, ApJL, 874, L6
Kataoka, A., Tsukagoshi, T., Momose, M., et al. 2016b, ApJL, 831, L12
Kataoka, A., Tsukagoshi, T., Pohl, A., et al. 2017, ApJL, 844, L5
Kirchschlager, F., Bertrang, G. H. M., & Flock, M. 2019, MNRAS, 488, 1211
Lazarian, A., & Hoang, T. 2007, ApJL, 669, L77
Lee, H. M., & Draine, B. T. 1985, ApJ, 290, 211
Liu, H. B. 2019, ApJL, 877, L22
Mathis, J. S., Rumpl, W., & Nordsieck, K. H. 1977, ApJ, 217, 425
Miyake, K., & Nakagawa, Y. 1993, Icar, 106, 20
Mori, T., Kataoka, A., Ohashi, S., et al. 2019, ApJ, 883, 16
Ohashi, S., Kataoka, A., Nagai, H., et al. 2018, ApJ, 864, 81
Okuzumi, S., & Tazaki, R. 2019, ApJ, 878, 132
Rebull, L. M., Wolff, S. C., & Strom, S. E. 2004, AJ, 127, 1029
Ricci, L., Testi, L., Natta, A., et al. 2010, A&A, 512, A15
Robitaille, T. P., Whitney, B. A., Indebetouw, R., & Wood, K. 2007, ApJS, 169, 328
Stephens, I. W., Looney, L. W., Kwon, W., et al. 2014, Natur, 514, 597
Stephens, I. W., Yang, H., Li, Z.-Y., et al. 2017, ApJ, 851, 55
Tamura, M., Hough, J. H., Greaves, J. S., et al. 1999, ApJ, 525, 832
Tamura, M., Hough, J. H., & Hayashi, S. S. 1995, ApJ, 448, 346
Tazaki, R., Lazarian, A., & Nomura, H. 2017, ApJ, 839, 56
Testi, L., Birnstiel, T., Ricci, L., et al. 2014, in Protostars and Planets VI, ed. H. Beuther et al. (Tucson, AZ: Univ. Arizona Press), 339
Warren, S. G., & Brandt, R. E. 2008, JGRD, 113, D14220
Yang, H., Li, Z.-Y., Looney, L., & Stephens, I. 2016, MNRAS, 456, 2794
Yang, H., Li, Z.-Y., Stephens, I. W., Kataoka, A., & Looney, L. 2019, MNRAS, 483, 2371
Zhu, Z., Zhang, S., Jiang, Y.-F., et al. 2019, ApJL, 877, L18